Ultra-Narrowband High-Transmissivity Guided-Mode Resonance Filter Based on Dual Dielectric Film Structure and High Refractive Index Waveguide Layer

Min Gao, Yu Zhang, Xinmiao Lu, Xiaoli Gong, and Lei Zheng

***Abstract*—In this study, we propose a novel approach to achieve an ultra-narrow bandwidth and high transmittance filter in the visible range. By employing TiO_2 as the waveguide layer material, the coupling energy in the waveguide layer is enhanced, leading to a reduction in the full width half maximum (FWHM). Additionally, a double-layer dielectric film structure composed of SiO_2 and Al_2O_3 is employed on the Ag grating to suppress random scattering leakage in the short wavelength range, resulting in reduced sidebands and improved transmittance of the resonant peak. To minimize wave loss between the metal grating and the waveguide layer, a SiO_2 dielectric layer is introduced. By adjusting the metal grating period, the resonance peak position can be shifted across the entire visible range. The proposed approach offers a metal grating-based guided-mode resonance (GMR) transmissive filter with low sidebands, high transmittance, ultra-narrow bandwidth, and tunability in the entire visible range. Experimental validation of the proposed design is conducted, and the results demonstrate the effectiveness of this approach in achieving superior filter performance in the visible spectral range.**

***Index Terms*—Guided mode resonance, subwavelength grating, ultra-narrowband, high-transmissivity, low sideband.**

I. Introduction

TRANSMISSIVE filters operating within the visible light range find diverse applications, such as spectral imaging [1], [2], [3], Complementary Metal Oxide Semiconductor (CMOS) image sensors [4], [5], biosensors [6], [7], and medical diagnostics [8]. Especially in the field of high spectral imaging, high-resolution spectral imaging plays a crucial role in applications such as cultural heritage research, object surveying, and person tracking [2]. Compared to multispectral imaging, high spectral imaging offers higher spectral resolution, enabling the capture of hundreds to thousands of spectral channels in the target wavelength range, thus acquiring continuous spectral information. Despite the growing demand for transmissive filters in the visible range [9], [10], [11], [12], [13], most studies have focused on reflection filters in the infrared band [14], [15], [16], [17], [18], [19]. Existing transmission filters in the visible range suffer from limitations including low diffraction efficiency, wide FWHM, and high sidebands, which lead to structural color issues such as reduced saturation and accuracy of color resolution. Compared with other filters, the waveguide structure of GMR breaks the diffraction limit and realizes light manipulation, while offering the advantages of high diffraction efficiency and extremely narrow FWHM [20], [21], [22]. This makes RGM filters one of the current hot topics.

Based on the fundamental principle of GMR [23], [24], [25], [26], [27], the combination of subwavelength gratings and GMR effects utilizes a periodic grating structure to ensure precise phase matching between the incident light and the intrinsic mode of the waveguide. This coupling mechanism enables the incident light that satisfies the phase match to be effectively coupled into the waveguide layer, surpassing the diffraction limit through the phenomenon of anomalous resonance [28]. As a result, a highly focused narrow-band resonance peak with remarkable transmission properties is generated. The resonance peak can be finely tuned by adjusting the parameters of the grating structure, offering control over the spectral characteristics of the device. In the work conducted by Daniel B. Mazulquim et al. [29] efficient and narrow-band transmission color filters were designed and fabricated, relying on a fundamental device consisting of an aluminum grating placed on a 200-nm-thick aluminum oxide film deposited on a glass substrate. Although the maximum transmittance exceeded 80%, it was accompanied by a sideband of more than 22% and a FWHM around 20 nm [29]. Wenze Wu et al. [30] designed a GMR matrix-based nanostructured transmission spectroscopy filter using a guided-mode resonance-type filter consisting of a metal grating, a SiO_2 buffer layer, and a high-emissivity waveguide layer. They employed the surface plasmon excitation mode of the metal grating, which was excited and coupled to the guided mode to achieve a low sideband sharp transmission peak of anomalous resonance, which was accompanied by a FWHM of 25 nm and a transmittance of only 70%, although his sideband was below 20% [30]. Guangyu Sun et al. [31] presented a tunable polarization-independent narrow-band GMR filter that employed a 2D subwavelength aluminum

Manuscript received 14 August 2023; revised 5 January 2024; accepted 17 February 2024. Date of publication 20 February 2024; date of current version 5 March 2024. This work was supported by the National Natural Science Foundation of China under Grant 62171172. *(Corresponding author: Yu Zhang.)*

The authors are with the School of Electronics and Information, Hangzhou Dianzi University, Hangzhou 310018, China (e-mail: 1424847305@qq.com; zy2009@hdu.edu.cn; xmlu@hdu.edu.cn; gxl@hdu.edu.cn; 1831980531@qq.com).

Digital Object Identifier 10.1109/JPHOT.2024.3367955

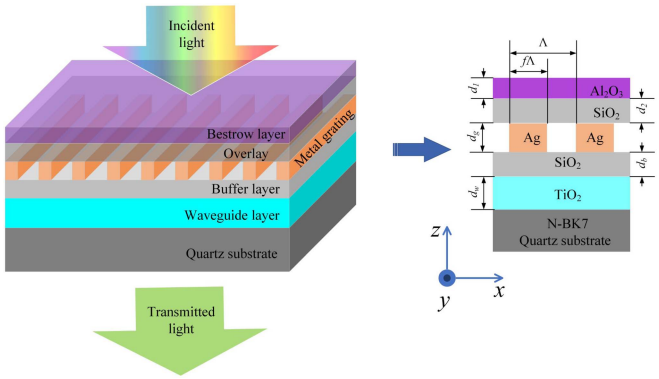

Fig. 1. Schematic diagram of multilayer metal gratings based GMR transmissive filter structure.

grating in conjunction with a polymer-dispersed liquid crystal layer. Although the transmittance reached 82.5%, the FWHM remained as high as 15 nm [31]. Xiangyu Ma et al. [32] designed a filter with periodic nanostructures and dielectric multilayers integrated on a silicon substrate. The filter has continuous tunability in the visible range (400 nm to 760 nm) with transmittance exceeding 75% but with 25% sidebands and FWHM higher than 15 nm, leaving room for further optimization [32]. These aforementioned studies have made significant progress in the development of transmission filters based on guided-mode resonance in the visible range and have made valuable contributions to the exploration of high-resolution, high-saturation color filters. Nonetheless, the resonance peaks still cannot simultaneously satisfy the extremely narrow FWHM, low sideband and high diffraction efficiency as well as the tunability in the entire visible range, which indicates that there is an unexplored potential for further improvement of transmissive GMR filters in the visible range.

The subwavelength grating structure encompasses various advantageous features, including a narrow bandwidth, high diffraction efficiency, good sideband suppression, and the capability to serve as a periodic structure for waveguide devices. Through the integration of the subwavelength grating structure with waveguide structures, it becomes feasible to achieve high transmission sharp resonance peaks. In this particular study, N-BK7 was employed as the substrate, Ag as the grating material, TiO_2 as the waveguide layer, and a dual dielectric layer comprising SiO_2 in conjunction with Al_2O_3 for anti-reflection coating., as depicted in Fig. 1. To mitigate the resonance bandwidth of the grating layer, a SiO_2 film is introduced as a buffer layer between the grating layer and the waveguide layer. The final transmittance of the designed device reaches about 80% with FWHM less than 4.2 nm and sidebands less than 18%. The distinguishing characteristics of the proposed structure are listed as follows:

1) Using the high-refractive-index material TiO_2 as the waveguide layer in the guided-mode resonant subwavelength grating structure, an ultra-narrow FWHM in the visible range can be achieved by exploiting the anomalous resonance mechanism of the high-refractive-index waveguide layer.
2) The top SiO_2 and Al_2O_3 films match the refractive index of the bottom layer and effectively suppress the sidebands by interaction, improving the peak transmittance and further narrowing the FWHM.

After optimization of the structural parameters, we succeeded in achieving high transmittance and low sideband. The transmittance can reach more than 80%, the sideband is suppressed to less than 20% and a very narrow transmission spectrum profile is obtained. The FWHM of the transmission spectrum is below 2.49 nm and can even reach 0.41 nm. Tunability of the transmission peaks throughout the visible band was achieved by adjusting the grating period parameters.

II. Model Building and Mechanisms

A. Model Building

This transmissive structure is one part of the imaging system, which is mainly used to receive the composite light reflected from objects in nature and resolve it into spectral information to provide monochromatic light information for the subsequent pixel module. To accurately analyze the output spectrum of plane light perpendicular to a metal-grating, we employed finite-difference time-domain method, to simulate the waveguide grating structure. The normal Y-polarized [33], [34] incident light propagates along the negative Z-direction, i.e., TE polarization. Periodic boundary conditions were imposed in the X- and Y-axis directions in the simulation region, while the upper and lower portions of the Z-axis were coated with perfect matching layers to eliminate echo interference. The thickness of each layer film is defined as d_1, d_2, d_g, d_b, d_w for the top layer (Al_2O_3), overlay (SiO_2), grating layer (Ag), buffer layer (SiO_2), and waveguide layer (TiO_2), respectively, and the period, duty cycle, and size ratio of the grating layer are defined as Λ, f, and $D = f\Lambda$ respectively. In order to determine the optimal thickness, we utilized the finite-difference time-domain method to systematically vary the thickness of each layer in the thin film and the duty cycle of the grating. By considering the combined effects of sidebands, transmittance, and FWHM, we carefully assessed the performance of the filters. Ultimately, the following parameters were selected for our study: a duty cycle of $f = 0.6$, a period of $\Lambda = 380$ nm, and specific thicknesses for each layer, namely $d_1 = 30$ nm $d_2 = 55$ nm, $d_g = 70$ nm, $d_b = 57$ nm, and $d_w = 100$ nm. The detailed parameter settings of the simulation software are shown in Table I. These optimized parameters were employed in the analysis of the subwavelength metal grating waveguide structure.

B. Mechanisms

Each layer plays an irreplaceable role in the entire structure. Next, we will analyze the role of each part in the structure from top to bottom.

Firstly, the dual dielectric film structure composed of SiO_2 and Al_2O_3 is used as an anti-reflection layer. Its effective refractive index is close to that of the substrate layer. This layer not only has the function of selectively transmitting the required light, but also effectively suppresses random scattering leakage

TABLE I
SIMULATION PARAMETER SETTING

Structural parameters	Numerical value	Simulation parameters	Numerical value
f	0.6	Mesh accuracy	6
Λ	300 nm	Boundary conditions	Periodic
d_1	30 nm	Incident light	A plane wave
d_2	55 nm	Polarization type	TE
d_g	70 nm	Angle of incidence	0°
d_b	57 nm	Z axis	PML
d_w	100 nm	---	---

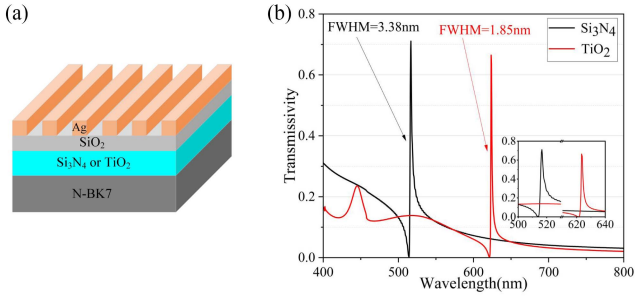

Fig. 2. (a) Fig. 1. Schematic diagram of a single-layer metal grating based GMR transmissive filter with Si_3N_4 or TiO_2 waveguide layer material. (b) Comparison of transmission spectra when the waveguide layer materials are Si_3N_4 and TiO_2, respectively.

in the short wavelength range, while enhancing the diffraction efficiency of the resonance peak.

Next, the grating layer plays the role of a periodically modulated layer in the structure, which is crucial for facilitating the transverse phase matching between the external wave and the waveguide mode, thus influencing the generation of guided mode resonance. Only by selecting appropriate duty cycle and thickness can the guided mode resonance effect be fully excited, thereby obtaining a narrow and tall transmission spectrum.

In addition to the grating layer and dual dielectric layer, the SiO_2 buffer layer in the structure also plays a vital role. Unlike in TM polarization, in TE polarization mode, when light transitions from the dielectric into the metallic layer, a phenomenon similar to plasmonics occurs. This resonant energy behaves like a plasmon and enters the waveguide layer, affecting the phase matching between the incident wave and the leaky modes in the waveguide layer, thus influencing the resonance of guided modes. In this case, the addition of the SiO_2 buffer layer effectively isolates this portion of energy from entering the waveguide layer, allowing for the efficient excitation of guided mode resonance and greatly reducing the full-width at half maximum.

Furthermore, the waveguide layer structure plays a crucial role in the entire configuration as it is an essential component for exciting the guided mode resonance phenomenon. When incident light irradiates the surface of the structure, it is coupled into the waveguide layer through the modulation of the grating layer to satisfy the phase matching condition between the inherent modes of the waveguide. However, since this portion of energy cannot be sustained entirely within the waveguide layer, leakage (referred to as leaky modes) occurs. The leaked energy interferes with the uncoupled light beam, resulting in the generation of reflectance and transmittance spectra.

Finally, the substrate layer is made of N-BK7 material, which was chosen due to its excellent transparency and corrosion resistance. Moreover, its refractive index matches that of the dual dielectric layer on top, allowing more light to pass through.

After understanding the specific roles of each layer, we will proceed to analyze this structure in detail using simulation software.

III. SIMULATION

A. Utilizing High Refractive Index Material TiO_2 As Waveguide Layer for FWHM Reduction

To facilitate efficient energy coupling into the waveguide layer, a high refractive index material is typically chosen for the waveguide layer. While Si_3N_4 is commonly used for this purpose, it still exhibits a relatively wide FWHM in the transmission spectra. To enhance energy coupling efficiency and reduce the FWHM, we selected TiO_2 as the waveguide layer material due to its higher refractive index (refractive index: 2.52–2.87) within the visible spectral range. By keeping other parameters fixed and solely altering the waveguide layer material, a comparative analysis was conducted. The structure diagram is shown in Fig. 2(a). Fig. 2(b) presents the transmission spectra comparison between Si_3N_4 and TiO_2 as waveguide layer materials. It is evident that the FWHM decreased from 3.38 nm to 1.85 nm when using TiO_2. Consequently, employing TiO_2 as the waveguide layer material, a high refractive index material, effectively narrows the FWHM and mitigates the reduces sidebands.

B. Enhancing Transmittance and Sideband Reduction in Grating-Based Filters Through Double Layer Dielectric Films: Al_2O_3 and SiO_2 Integration

In order to comprehensively analyze the impact of the structural parameters of the bilayer dielectric layer on the output spectrum of guided GMR transmission filters based on a metal grating, we conducted investigations on the transmission spectra with and without SiO_2 and Al_2O_3 film layers.

Initially, we examined the transmission spectra without the double-layer dielectric film structure by varying the grating period Λ (165 nm to 385 nm) within the visible range. Fig. 3(a) illustrates the transmittance as a function of grating period and wavelength λ. Fig. 3(b) compares the transmission spectra for different grating periods, revealing the presence of higher sidebands in the short wavelength band due to random scattering leakage. Importantly, as the grating period exceeds 300 nm, the

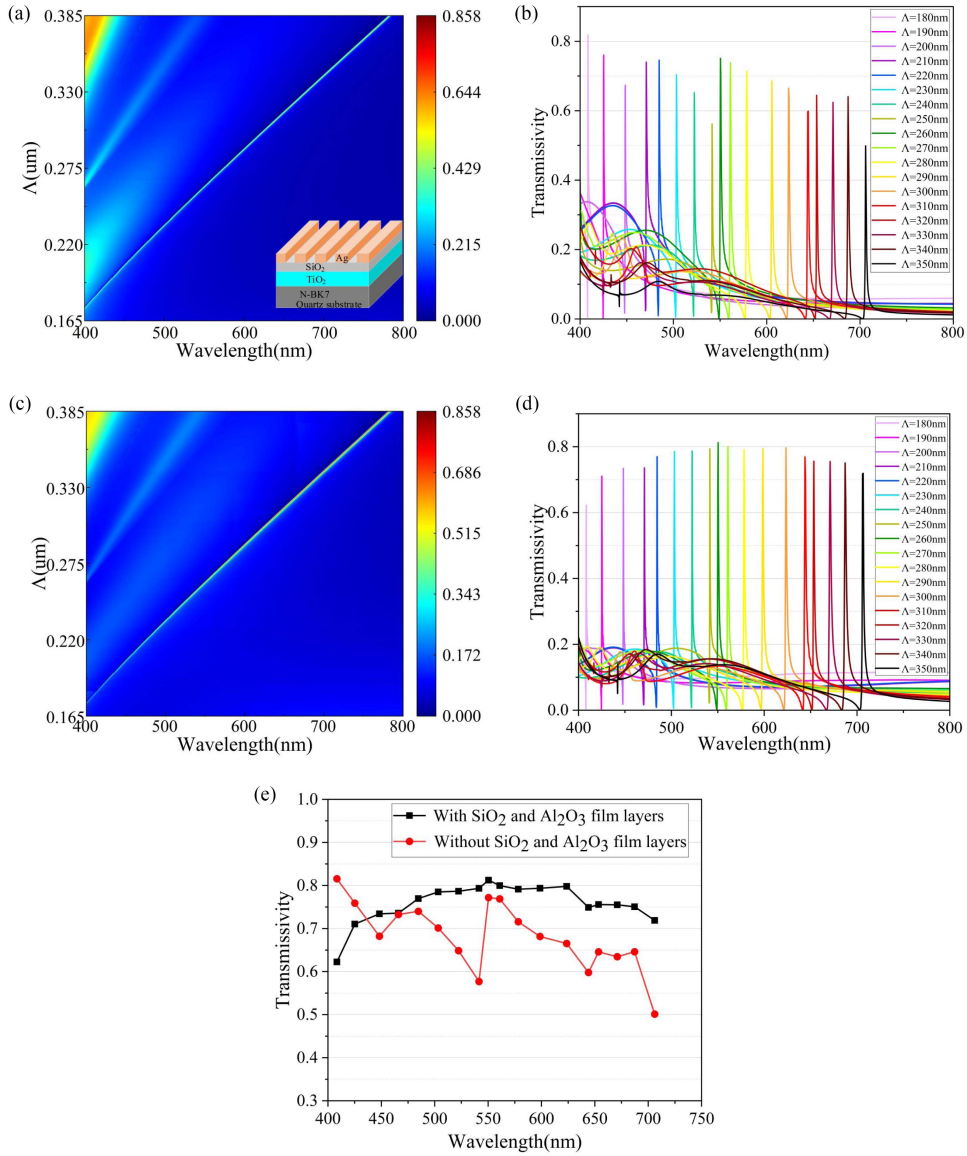

Fig. 3. (a) Reference view of grating size scan of bilayer dielectric film without SiO_2 and Al_2O_3 addition. (b) Transmittance spectra corresponding to the variation of grating period Λ from 180–350 nm. (c) Reference view of grating size scan of bilayer dielectric film with SiO_2 and Al_2O_3 addition. (d) Transmittance scan parameter plot when the grating period Λ is varied from 180–350 nm. (e) Transmittance comparison curves at the peak positions of the two grating structures.

peak transmission intensity gradually decreases, leading to a decline in filter performance. Therefore, our objective is to enhance diffraction efficiency, minimize sidebands, and decrease the FWHM within the visible range. To achieve these goals, we have systematically scanned the period Λ from 180 nm to 400 nm for metal gratings with the addition of a double dielectric film. Fig. 3(c) depicts the transmittance versus period Λ for the subwavelength guided-mode resonant metal grating structure, demonstrating effective tunability of the resonant peak position through adjustment of the period parameter. By comparing the results in Fig. 3(a) and (c) (For comparison purposes, the maximum value of the color-coded caliper in Fig. 3(a) was modified from 0.782 to the same 0.858 as in Fig. 3(c)), it is evident that the introduction of a double-layer dielectric film structure successfully suppresses scattering losses and improves energy convergence. Fig. 3(d) highlights the advantages of the additional double dielectric film on the grating, including a significant reduction in sidebands to less than 20%, an increase in peak transmittance to 82%, and a further decrease in FWHM, resulting in a high-quality factor Q. Importantly, the resonant peak-to-peak position remains largely unaffected. Fig. 3(e) demonstrates that the transmittance of the bilayer dielectric film structure consistently hovers around 80%, while the transmittance is generally lower without the bilayer dielectric film structure. This indicates that the double-layer dielectric film structure effectively suppresses random scattering leakage in the short wavelength band while enhancing energy convergence in the waveguide layer. We compared our designed transmission-type filter with the existing structures, and the specific data are shown in Table II. In the table, T denotes the transmittance and T_s denotes the sideband height. As can be seen from Table II, in the visible wavelength band, our designed transmission-type filter overcomes the shortcomings of existing studies that cannot satisfy narrow FWHM, low sideband, and high diffraction

TABLE II
PERFORMANCE DATA OF THE PROPOSED NARROW-BAND GRATING FILTER AND OTHER PROPOSED FILTERS

Categorization	FWHM (nm)	T (%)	T_s (%)	Simulated or Measured
Daniel B. Mazulquim's in [29]	20	**80**	22	Simulated
Wenze Wu's in [30]	25	70	20	Simulated
Guangyu Sun's in [31]	15	**82.5**	---	Simulated
Xiangyu Ma's in [32]	15	75	25	Simulated
In this study	**1.6**	**79.8**	**17.8**	Simulated

The bold font indicates the performance index parameters of the proposed structure, as well as some parameters in the existing studies with higher performance index than that of the proposed structure.

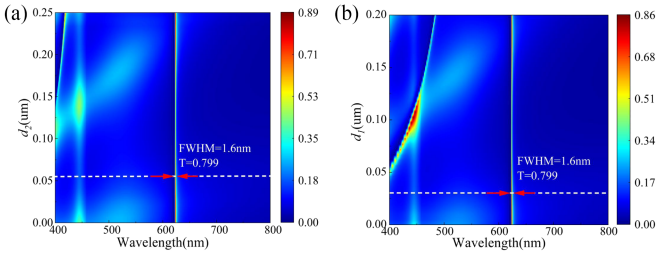

Fig. 4. (a) Transmittance scan of the resonance center wavelength λ with the thickness of SiO_2 film d_2 is changing from 0 to 0.25 um when the thickness of Al_2O_3 is 30 nm. (b) Transmittance scan of the resonance center wavelength λ with the thickness of Al_2O_3 film d_1 is changing from 0 to 0.25 um when the thickness of SiO_2 is 55 nm.

efficiency at the same time. Consequently, this approach improves color saturation in the visible range and significantly enhances the performance of the transmission filters.

Furthermore, to investigate the specific effect of SiO_2 and Al_2O_3 bilayer films on the response, we simulated the transmission spectra of the resonant center wavelength λ with the thickness of SiO_2 when the thickness of Al_2O_3 is 30 nm, and the transmission spectra of the resonant center wavelength λ with the thickness of Al_2O_3 when the thickness of SiO_2 is 55 nm, as depicted in Fig. 4(a) and Fig. 4(b), it is evident that the height of the short wavelength sidebands is influenced by the double-layer dielectric film above the grating. Specifically, when the thicknesses of SiO_2 and Al_2O_3 films are set to 55 nm and 30 nm, respectively, the high sidebands of the short wavelength sidebands are significantly reduced, whileav maintaining resonant peak-to-peak transmission above 80%. Therefore, the double-layer dielectric film structure composed of SiO_2 and Al_2O_3 can effectively suppress random scattering leakage in the short wavelength range, indicating a direct correlation between the presence or absence of the double-layer dielectric film structure and the change trend of sidebands in the short wavelength range of this structure. Opting for appropriate thicknesses of SiO_2 and Al_2O_3 film layers can not only suppress the height of the sidebands but also increase peak transmittance at resonant wavelengths to around 80%, while reducing FWHM to 1.6 nm.

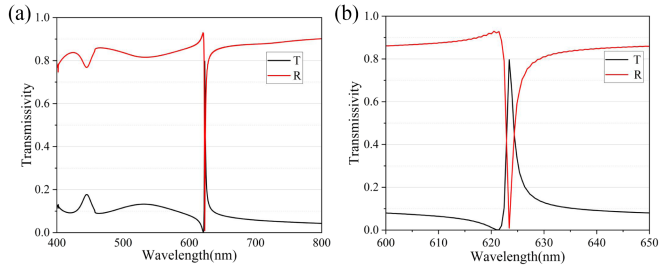

Fig. 5. (a) Comparison curves of transmission and reflection for grating size Λ = 300 nm. (b) Partial enlarged view in Fig. 5(a).

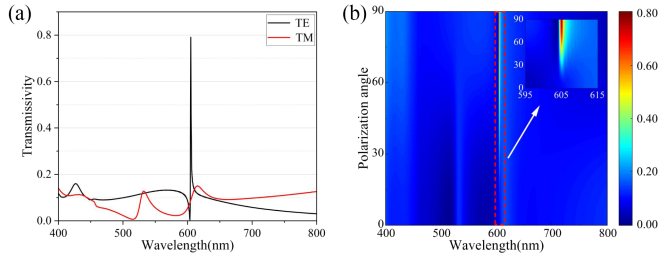

Fig. 6. (a) Transmission spectra when the incident light is TE and TM polarized. (b) Plot of the sweep parameters of the polarization angle.

C. High Quality Factor

The transmission and reflection spectra at this resonant frequency were investigated as shown in Fig. 5(a), which shows the comparison of transmittance and reflectance for the grating cycle Λ = 300 nm, with the resonant center wavelength at 623.401 nm. Fig. 5(b) is a partial enlargement of Fig. 5(a). The high reflectance at non-resonant wavelengths still indicates that the structure is capable of achieving narrowband filters with a high-quality factor Q ($Q = \lambda/\Delta\lambda$, $\Delta\lambda$), denotes the FWHM), which is suitable for applications of transmission filters in the visible range. Table III displays the FWHM and quality factor Q data for 18 different grating periods. From Table III, we can observe that the FWHM values consistently remain within the range from 0.41 nm to 2.5 nm. Additionally, the grating structures exhibit the remarkably high-quality factor Q, reaching a maximum value of 984.048. It is difficult to obtain high-quality factor Q from a structure with poor energy coupling efficiency, so by changing the structural dimensions of the filter, more energy can be gathered in the waveguide layer, thus increasing the energy coupling efficiency, which in turn increases the quality factor Q of the transmitted spectrum.

D. Polarization Property

Last but not least, the impact of the polarization angle on the transmission spectrum was also examined. Specifically, a fixed subwavelength metal grating period cycle Λ of 295 nm was utilized, and the polarization angle was scanned. The scanning results are presented in Fig. 6 It was observed that, as the polarization angle increased, the position of transmission peak is almost unshifted, and the peak intensity decreased considerably. A comparison of the transmission spectra of TE and TM polarized light showed that the transmittance in TE polarized

TABLE III
CENTER WAVELENGTH, FWHM, TRANSMISSIVITY AND QUALITY FACTOR Q CORRESPONDING TO DIFFERENT GRATING CYCLE Λ

Λ(nm)	Center wavelength (nm)	FWHM (nm)	Transmissivity (%)	Quality factor
180	408.380	0.415	62.249	984.048
190	425.106	0.550	71.041	772.920
200	448.233	0.503	73.418	891.119
210	466.000	0.700	73.584	665.714
220	484.657	0.867	76.973	559.005
230	503.275	0.959	78.513	524.791
240	522.353	0.720	78.661	725.490
250	541.463	0.700	79.343	773.519
260	*550.413*	1.120	81.233	491.440
270	560.842	1.330	79.978	421.686
280	578.292	1.500	79.136	385.528
290	598.652	1.500	79.351	399.101
300	623.401	1.600	79.789	389.625
310	643.997	1.801	74.895	357.577
320	653.475	1.530	75.580	427.108
330	671.033	2.326	75.513	288.492
340	687.188	2.269	75.053	302.860
350	706.007	2.491	71.901	283.423

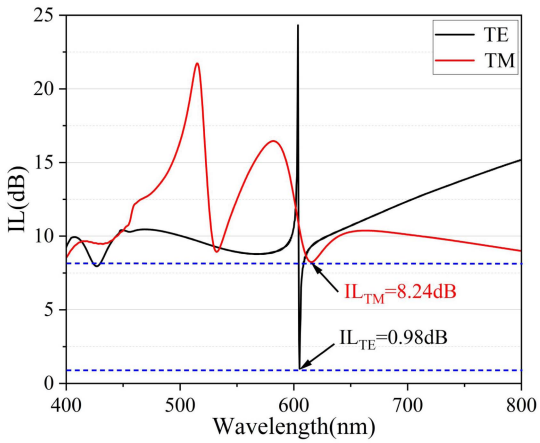

Fig. 7. Insertion loss plot for TE vs. TM polarization.

light was 0.8, while the transmittance in TM polarized light rapidly decreased to approximately 0.13, generating a significant difference. We also analyzed the insertion loss of the proposed structure in TE and TM polarization modes, as shown in Fig. 7 At the resonance wavelength of 204.996 nm, the insertion loss for TE polarization wave is only 0.98 dB, while the insertion loss for TM polarization wave is as high as 8.24 dB. This structure has potential applications in polarization separation fields.

IV. DISCUSSION

In metal grating waveguide structures, guided-mode resonances occur due to the coupling between the grating diffraction wave and the waveguide mode of the high-refractive-index waveguide layer. This coupling leads to the generation of a highly pronounced resonant peak at the resonant wavelength when the diffracted optical field aligns with the higher-order diffracted waves and the waveguide leakage mode. By adjusting the grating cycle Λ, it becomes possible to achieve sharp spikes in the visible range, accompanied by a noticeable red shift of the transmission resonance peak as the grating cycle Λ increases. This alteration in physical dimensions causes a shift in the resonance center of the guided-mode resonance, consequently affecting the ultimate imaging of the transmission spectrum. To gain a deeper understanding of the physical mechanism behind the generation of resonance peaks, we conducted an analysis of the electric field distribution on the XOZ plane at the peak position. Since the resonance mechanisms at different resonance peaks are fundamentally the same, it suffices to focus on one specific resonance point. Fig. 8(a)–(c) depict the transmission spectra corresponding to different structural parameters for a grating period Λ of 300 nm, from which it can be seen that these filters exhibit a single transmission peak in the visible range with resonance wavelengths λ of 517.603 nm, 623.401 nm and 623.401 nm, respectively. In Fig. 8(d)–(f), we plot the point field distribution in the XOZ plane corresponding to the peak positions of the different structures in Fig. 8(d)–(f), respectively. Points A_1, A_2, and A_3 represent the maximum value of energy converged within the waveguide layer, while points B_1, B_2, and B_3 represent the energy distribution outside the waveguide layer. The smaller the energy outside the waveguide layer, the less scattering energy loss is indicated.

A. Discussion of Utilizing High Refractive Index Material TiO_2 As Waveguide Layer for FWHM Reduction

To investigate the physical mechanism underlying the narrower full width at half maximum (FWHM) achieved by utilizing the high refractive index material TiO_2 as the waveguide layer,

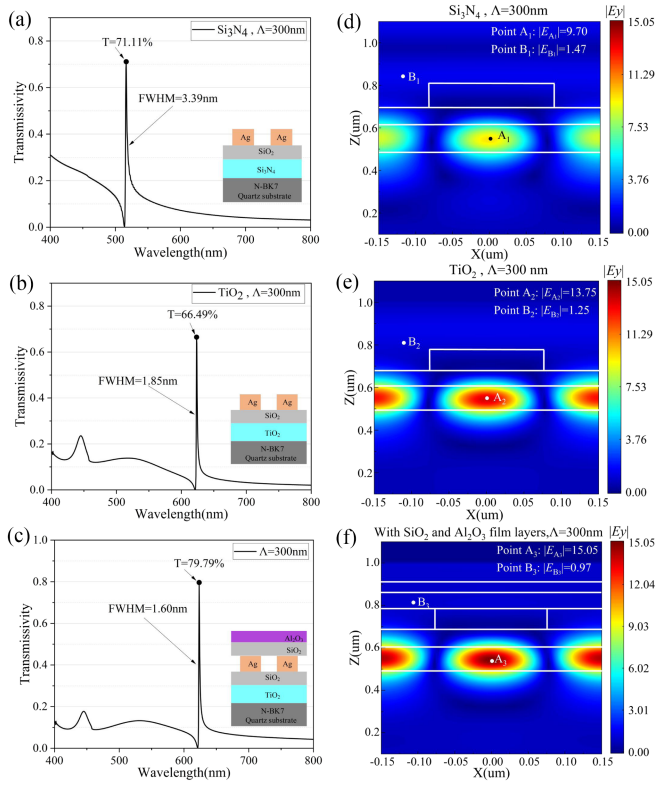

Fig. 8. (a)–(c) Transmission spectra at different structural parameters when the period is 300 nm. (d)–(f) When the resonance peaks are $\lambda = 571.603$ nm, $\lambda = 623.401$ nm, and $\lambda = 623.401$ nm, the magnetic field distribution corresponding to the structures in Figs. 8(a)–(c).

we conducted an analysis of the XOZ plane electric field distribution at the resonance peaks of 517.603 nm and 623.401 nm in the structures depicted in Fig. 8(a) and Fig. 8(b) respectively. The electric field distributions are shown in Fig. 8(d) and (e) respectively. By comparing the values at point A_1 ($|E_{A1}| = 9.70$) and B_1 ($|E_{B1}| = 1.47$) in Fig. 6(d) with the values at point A_2 ($|E_{A2}| = 13.75$) and B_2 ($|E_{B2}| = 1.25$) in Fig. 8(e), along with the corresponding electric field energy distribution in the XOZ plane, it becomes evident that the utilization of TiO_2 as the waveguide layer, with its high refractive index, leads to a more concentrated energy convergence within the waveguide layer. This results in larger electric field energy and stronger energy coupling capability, ultimately leading to a significant reduction in the FWHM.

B. Discussion of Double Layer Dielectric Films SiO_2 and Al_2O_3 to Reduce Sidebands and Improve Transmittance

To elucidate the mechanism of action of the bilayer dielectric film structure comprising SiO_2 and Al_2O_3, we conducted an analysis of the XOZ planar electric field distribution at the resonance peak of 623.401 nm in the structure illustrated in Fig. 8(c), employing the same method as described in Section IV-A. The obtained results are presented in Fig. 8(f). By comparing the values at points A_2 ($|E_{A2}| = 13.75$) and B_2 ($|E_{B2}| = 1.25$) in Fig. 8(e) with the values at points A_3 ($|E_{A3}| = 15.05$) and B_3 ($|E_{B3}| = 0.97$) in Fig. 8(f), along with

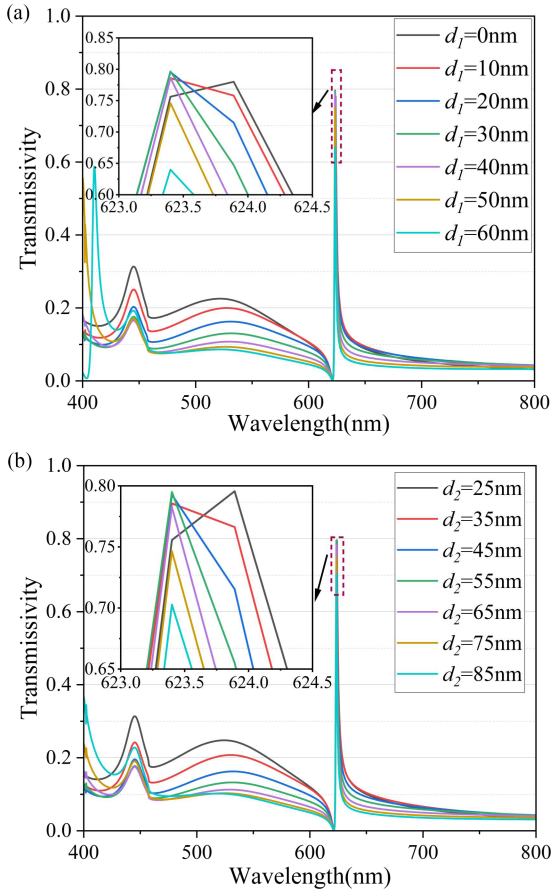

Fig. 9. (a) Transmittance profile for variation of Al_2O_3 thickness. (b) Transmittance profile for variation of SiO_2 thickness.

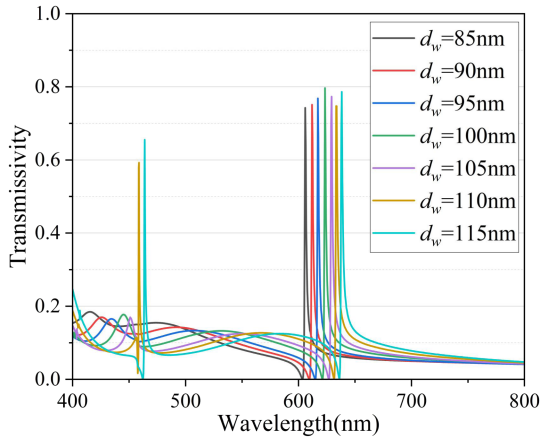

Fig. 10. Transmittance profile for variation of TiO_2 thickness.

considering the corresponding electric field energy distribution in the XOZ plane, it can be inferred that the introduction of SiO_2 and Al_2O_3 leads to a reduction of energy in the outer region of the waveguide layer. This reduction demonstrates that the structure effectively suppresses the random scattering leakage of energy, as well as enhances the energy convergence and the energy coupling efficiency within the waveguide layer, thus consequently contributing to the decrease in sidebands and the increase in peak transmittance.

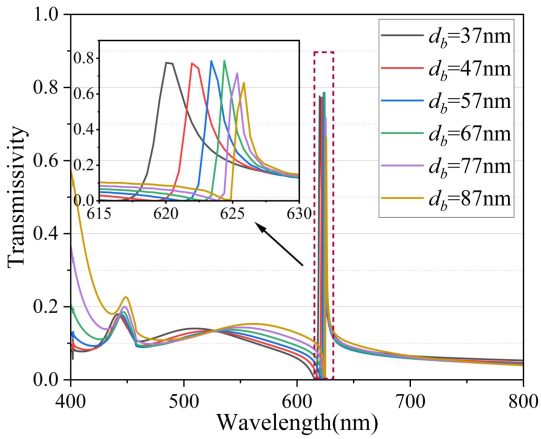

Fig. 11. Transmittance profile for variation of SiO_2 thickness.

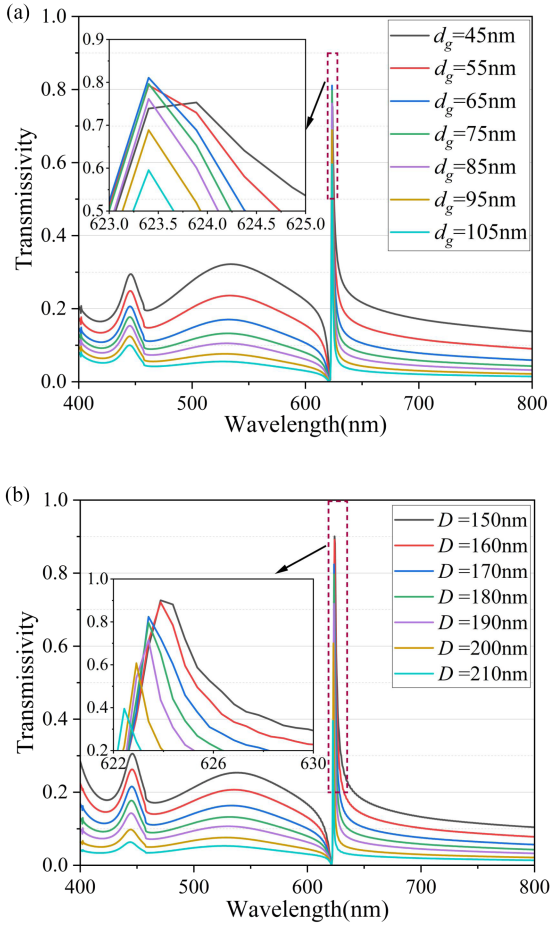

Fig. 12. (a) Transmittance profile when Ag thickness is varied. (b) Transmittance profile when Ag width is varied.

C. Discussion of the Effect of Film Parameters on Transmission Spectra for Each Layer

In order to investigate the influence of SiO_2 and Al_2O_3 bilayer film thickness on the response, we conducted simulations of the transmission spectra when the Al_2O_3 thickness was set at 30 nm with varying SiO_2 thickness, as well as when the SiO_2 thickness was set at 55 nm with varying Al_2O_3 thickness, as shown in Fig. 9(a) and (b) respectively. From Fig. 9(a) and (b), it can be observed that within the range of 20 nm–40 nm, the transmission waveforms of the Al_2O_3 film exhibit minimal changes, while for thicknesses below 20 nm, the waveforms exhibit higher sidebands, and for thicknesses above 40 nm, the transmission rate significantly decreases, with higher order peaks appearing in the short wavelength region. Similarly, when the SiO_2 thickness varies within the range of 45–65 nm, there is minimal impact on the transmission waveforms. However, for thicknesses below 20 nm, the waveforms exhibit higher sidebands, and for thicknesses above 40 nm, the sidebands of the waveforms increase sharply, with a significant decrease in the transmission rate. Therefore, selecting appropriate thicknesses for the SiO_2 and Al_2O_3 layers allows for the suppression of the sidebands height, while increasing the peak transmission rate at the resonant wavelength to around 80% and reducing the FWHM to 1.6 nm.

Similarly, we also simulated the effect of the waveguide layer thickness on the transmission spectra, as shown in Fig. 10. From Fig. 10, it can be observed that as the waveguide layer thickness increases, the transmission spectrum undergoes a red shift, which can be corrected by compensating for the optical path difference. The transmission rate in the graph shows an upward trend, while the sidebands exhibit a downward trend. When the waveguide layer thickness increases to 100 nm, the transmission rate reaches a maximum of 79.8%. However, as the waveguide layer thickness continues to increase, the transmission rate gradually decreases. At a thickness of 110 nm, a strong side peak appears in the short wavelength region, which is caused by the fulfillment of multiple phase matching conditions.

We also simulated the transmission spectra of the SiO_2 buffer layer and compared the results before and after adding the SiO_2 buffer layer, as shown in Fig. 11. In Fig. 11, we found that with an increase in the thickness of the buffer layer, there is a slight redshift in the resonance center, a significant decrease in the FWHM of the transmission peak, and the transmission rate remains around 79.8%, with sidebands consistently below 18%. However, when the thickness of the SiO_2 buffer layer increases to 67 nm, the peak transmission rate decreases, and the sidebands in the short wavelength region increase sharply, severely affecting the extraction of spectral information.

Next, we investigated the effect of parameter changes in the grating layer on the transmission spectra. To clarify the effects of grating layer thickness and width ($D = f\Lambda$, $\Lambda = 300$ nm), we simulated the grating layer thickness and duty cycle separately, as shown in Fig. 12. From the figures, it can be observed that when the grating thickness is less than 65 nm or the width D is less than 0.155 nm ($f = 0.563$), it leads to weak excitation of guided mode resonance, resulting in high sidebands in the transmission spectra. As the grating thickness and duty cycle increase, a strong guided mode resonance effect is generated, resulting in narrow and tall transmission peaks. However, when the grating parameters continue to increase to a thickness over 85 nm or width D reaches 190 nm ($f = 0.634$), it significantly affects the transmittance of Ag, leading to a significant decrease in peak transmission rate.

TABLE IV
INSERTION LOSS, FWHM, TRANSMITTANCE AND SIDEBANDS CORRESPONDING TO DIFFERENT THICKNESSES OF EACH LAYER, AS WELL AS MANUFACTURING TOLERANCES FOR EACH LAYER

	h (nm)	IL (dB)	FWHM (nm)	T (%)	T_s (%)	Δd (nm)
d_w	95	1.11	1.4	77.4	16.4	±5
	100	**0.97**	**1.6**	**79.8**	**17.8**	
	105	1.08	1.7	77.9	17.2	
d_b	47	1.01	1.7	79.2	20.1	±10
	57	**0.97**	**1.6**	**79.8**	**17.8**	
	67	0.98	1.5	79.7	17.5	
d_2	45	0.98	1.6	79.7	19.8	±10
	55	**0.97**	**1.6**	**79.8**	**17.8**	
	65	1.04	1.5	78.6	17.9	
d_1	20	0.99	1.6	79.6	20.2	±10
	30	**0.97**	**1.6**	**79.8**	**17.8**	
	40	1.03	1.5	78.8	17.5	
d_g	65	0.96	1.7	80.1	20.2	±10
	75	**0.97**	**1.6**	**79.8**	**17.8**	
	85	1.03	1.6	78.9	15.5	
D	170	0.96	1.6	81.7	21.8	±10
	180	**0.97**	**1.6**	**79.8**	**17.8**	
	190	1.03	1.5	75.9	14.1	

The bold font indicates the optimal structural parameter values of the proposed structure, as well as the device performance index parameter values corresponding to the optimal structural parameter values.

In summary, the optimal parameters of the structure at the resonance wavelength $\lambda = 623.401$ nm can be determined as: a duty cycle of $f = 0.6$, a period of $\Lambda = 380$ nm, and specific thicknesses for each layer, namely $d_1 = 30$ nm $d_2 = 55$ nm, $d_g = 70$ nm, $d_b = 57$ nm, and $d_w = 100$ nm. Considering that a certain degree of dimensional error is inevitably introduced during the manufacturing process, we determined appropriate manufacturing tolerances based on the impact of different layer parameter variations on the waveform data in Figs. 9 to 12. Our conclusions are as follows: the manufacturing tolerance of the waveguide layer is 10 nm, the allowed manufacturing tolerance Δd for the thickness of other layers is 20 nm, and the allowed manufacturing tolerance for duty ratio is 0.563–0.634 ($D =$ 170 nm–190 nm). We also calculated the insertion loss values, where Po represents the transmitted energy and Pi represents the input energy) for each layer thickness variation based on the transmittance at the resonance peak position. The final results are summarized in Table IV. In the table, IL represents insertion loss, h represents the thickness of each layer, T represents transmittance, T_s represents sideband height, and Δd represents the allowed manufacturing tolerance.

V. CONCLUSION

In this study, we propose a subwavelength metal grating structure that harnesses guided-mode resonance to achieve precise adjustment of a single transmission peak throughout the visible spectrum. Through simulation and comparison of waveguide layer structures utilizing high refractive index material TiO_2 and low refractive index material Si_3N_4, we observe that TiO_2 enhances energy coupling capability within the waveguide layer. Furthermore, by simulating two waveguide metal grating configurations with and without the incorporation of double dielectric films (Al_2O_3 and SiO_2) above the grating, we find that the double film structure effectively suppresses short-wavelength sideband transmission and increases the intensity of the transmission peak in the long-wavelength region. In summary, the proposed structure not only achieves an impressive 80% transmittance at the resonance wavelength, but also provides narrow-band filters with a high-quality factor Q of up to 850 in the visible range, accompanied by an FWHM less than 2.49 nm. This represents a noteworthy advancement for transmittance filters operating in the visible range.

ACKNOWLEDGMENT

All material refractive indices are from the website RefractiveIndex. INFO. Data underlying the results presented in this paper are not publicly available at this time but maybe obtained from the authors upon reasonable request.

REFERENCES

[1] X. Wang, Y. Zhang, X. Ma, T. Xu, and G. R. Arce, "Compressive spectral imaging system based on liquid crystal tunable filter," *Opt. Exp.*, vol. 26, no. 19, pp. 25226–25243, Jan. 2018.
[2] R. Hahn, T. Haist, K. Michel, and W. Osten, "Diffraction-based hyperspectral snapshot imager," *Opt. Eng.*, vol. 61, no. 1, pp. 15106, Jul. 2022.
[3] Y. Saita, D. Shimoyama, R. Takahashi, and T. Nomura, "Single-shot compressive hyperspectral imaging with dispersed and undispersed light using a generally available grating," *Appl. Opt.*, vol. 61, no. 5, pp. 1106–1111, Feb. 2022.
[4] Y. Zhu, X. Lei, K. X. Wang, and Z. Yu, "Compact CMOS spectral sensor for the visible spectrum," *Photon. Res.*, vol. 7, no. 9, Sep. 2019, Art. no. 961.
[5] J. Berzinš, S. Fasold, T. Pertsch, S. M. B. Bäumer, and F. Setzpfandt, "Submicrometer nanostructure-based RGB filters for CMOS image sensors," *ACS Photon.*, vol. 6, no. 4, pp. 1018–1025, 2019.
[6] H. Altug, S. Oh, S. A. Maier, and J. Homola, "Advances and applications of nanophotonic biosensors," *Nature Nanotechnol.*, vol. 17, no. 1, pp. 5–16, 2022.
[7] D. Rho, C. Breaux, and S. Kim, "Label-free optical resonator-based biosensors," *Sensors-Basel*, vol. 20, no. 20, Sep. 2020, Art. no. 5901.
[8] C. G. Stefanita, Y. F. Shao, W. Rozmus, C. E. Capjack, and C. J. Backhouse, "Filtering scattered light in microchip-based cell diagnostics," *IEEE T. Instrum. Meas.*, vol. 54, no. 5, pp. 2093–2098, Oct. 2005.
[9] E. Buhara, A. Ghobadi, and E. Ozbay, "Adaptive visible and short-wave infrared camouflage using a dynamically tunable metasurface," *Opt. Lett.*, vol. 46, no. 19, pp. 4777–4780, Oct. 2021.
[10] J. M. Foley and J. D. Phillips, "Normal incidence narrowband transmission filtering capabilities using symmetry-protected modes of a subwavelength, dielectric grating," *Opt. Lett.*, vol. 40, no. 11, pp. 2637–2640, Jun. 2015.
[11] C. H. Park, Y. T. Yoon, and S. S. Lee, "Polarization-independent visible wavelength filter incorporating a symmetric metal-dielectric resonant structure," *Opt. Exp.*, vol. 20, no. 21, pp. 23769–23777, Oct. 2012.
[12] L. Wang, T. Sang, J. Gao, X. Yin, and H. Qi, "High-performance sensor achieved by hybrid guide-mode resonance/surface plasmon resonance platform," *Appl. Opt.*, vol. 57, no. 25, pp. 7338–7343, Sep. 2018.
[13] S. S. Wang and R. Magnusson, "Multilayer waveguide-grating filters," *Appl. Opt.*, vol. 34, no. 14, pp. 2414–2420, 1995.
[14] C. Wang et al., "Full-color reflectance-tunable filter based on liquid crystal cladded guided-mode resonant grating," *Opt. Exp.*, vol. 30, no. 13, pp. 22820–22829, Oct. 2022.

[15] Y. Zhao et al., "Multi-layered all-dielectric grating visible colorfilter with a narrow band and high-quality factor," *Opt. Exp.*, vol. 30, no. 13, pp. 22820–22829, Jun. 2022.
[16] S. Feng, Y. Liao, and Y. Zhao, "Graphene-based tunable bandpass guided-mode resonance mid-infrared filter," *Mod. Phys. Lett. B*, vol. 33, no. 30, pp. 1950360–1950367, 2019.
[17] M. Shyiq Amin, J. Woong Yoon, and R. Magnusson, "Optical transmission filters with coexisting guided-mode resonance and Rayleigh anomaly," *Appl. Phys. Lett.*, vol. 103, no. 13, 2013, Art. no. 131106.
[18] S. Schoenhardt, A. Boes, T. G. Nguyen, and A. Mitchell, "Ridge waveguide couplers with leaky mode resonator-like wavelength responses," *Optik*, vol. 121, no. 12, pp. 1144–1147, Jan. 2010.
[19] J. Ma et al., "Transmission guided-mode resonance filters based on high reflection multilayer stacks," *Optik*, vol. 121, no. 12, pp. 1144–1147, Dec. 2010.
[20] C. Tuambilangana, F. Pardo, E. Sakat, P. Bouchon, J. Pelouard, and R. Haïdar, "Two-mode model for metal-dielectric guided-mode resonance filters," *Opt. Exp.*, vol. 28, no. 22, 2020, Art. no. 32456.
[21] R. He, C. Chen, R. Zhang, L. Chen, and J. Guo, "Dual dielectric cap gold nanoslits array optical resonance filter with large figure-of-merit," *Opt. Exp.*, vol. 28, no. 22, Oct. 2020, Art. no. 32456.
[22] J. Jin, X. Yin, L. Ni, M. Soljačić, B. Zhen, and C. Peng, "Topologically enabled ultrahigh-Q guided resonances robust to out-of-plane scattering," *Nature*, vol. 574, no. 7779, pp. 501–504, Oct. 2019.
[23] D. A. Bykov and L.L. Doskolovich, "Spatiotemporal coupled-mode theory of guided-mode resonant gratings," *Pt. Exp.*, vol. 23, no. 15, 2015, Art. no. 19234.
[24] L. Qian, T. Gu, S. Xu, X. Zhang, and K. Wang, "Guided-mode resonance sensors with ultrahigh bulk sensitivity and figure of merit assisted by a metallic layer and structural symmetry-breaking," *Opt. Exp.*, vol. 31, no. 2, pp. 1844, Jan. 2023.
[25] M. Maleki and M. Mehran, "Guided-mode resonance sensors: Different schemes for different applications," *Opt. Lett.*, vol. 47, no. 18, pp. 4704–4707, Sep. 2022.
[26] K. Zhou, X. Sun, H. Ma and X. Zhong, "Theoretical demonstration of tunable multichannel midinfrared optical filters for infrared spectroscopic gas detection," *IEEE Sens. J.*, vol. 23, no. 4, pp. 3567–3572, Feb. 2023.
[27] D. Rout, P. Venkatachalam, R. Singh, L. P. Shree, and S. K. Selvaraja, "Guided mode resonance aided polarization insensitive in-plane spectral filters for an on-chip spectrometer," *Opt. Lett.*, vol. 47, no. 18, pp. 4704–4707, Sep. 2022.
[28] S. Nemcova, V. Havran, and J. Hosek, "Different view on diffraction-limited imaging optics design," *J. Opt. Soc. Amer. A Opt. Image Sci. Vis.*, vol. 40, no. 1, pp. 149–154, Jan. 2023.
[29] D. B. Mazulquim et al., "Efficient band-pass color filters enabled by resonant modes and plasmons near the Rayleigh anomaly," *Opt. Exp.*, vol. 22, no. 25, 2014, Art. no. 30843.
[30] W. Wu et al., "Nano-structured transmissive spectral filter matrix based on guided-mode resonances," *J. Eur. Opt. Soc.-Rapid*, vol. 15, no. 1, 2019, Art. no. 19.
[31] G. Sun and Q. Wang, "Electrically tunable polarization-independent visible transmission guided-mode resonance filter based on polymer-dispersed liquid crystals," *Microw. Opt. Techn. Let.*, vol. 62, no. 12, pp. 3727–3732, Jan. 2020.
[32] X. Ma, Y. Zhai, J. Ji, Z. Wu, and Q. Wang, "The optical properties of a visible light filter integrated on the silicon substrate," *Opt. Commun.*, vol. 464, Feb. 2020, Art. no. 125510.
[33] E. MorenoL. Martín-Moreno and F.J. García-Vidal, "Extraordinary optical transmission without plasmons: The s-polarization case," *J. Opt. A, Pure Appl. Opt.*, vol. 8, no. 4, pp. S94–S97, Mar. 2006.
[34] Z. ZhanJ. WeiY. Miao and Q. Wang, "Polarization-Independent Narrowband Terahertz Filter Based on All-Dielectric Metasurfaces," *IEEE Photon. J.*, vol. 15, no. 2, Apr. 2023, Art. no. 4600606.